Title

Direct imaging of short-range order and its impact on deformation in Ti-6Al.

Journal

Science advances, 5(12)

ISSN

2375-2548

Authors

Zhang, Ruopeng
Zhao, Shiteng
Ophus, Colin
et al.

Publication Date

2019-12-01

DOI

10.1126/sciadv.aax2799

Peer reviewed

MATERIALS SCIENCE

Direct imaging of short-range order and its impact on deformation in Ti-6Al

Ruopeng Zhang[1,2]*, Shiteng Zhao[1,2]*, Colin Ophus[2], Yu Deng[3], Shraddha J. Vachhani[4], Burak Ozdol[2], Rachel Traylor[1,2], Karen C. Bustillo[2], J. W. Morris Jr.[1], Daryl C. Chrzan[1,5], Mark Asta[1,5], Andrew M. Minor[1,2†]

Chemical short-range order (SRO) within a nominally single-phase solid solution is known to affect the mechanical properties of alloys. While SRO has been indirectly related to deformation, direct observation of the SRO domain structure, and its effects on deformation mechanisms at the nanoscale, has remained elusive. Here, we report the direct observation of SRO in relation to deformation using energy-filtered imaging in a transmission electron microscope (TEM). The diffraction contrast is enhanced by reducing the inelastically scattered electrons, revealing subnanometer SRO-enhanced domains. The destruction of these domains by dislocation planar slip is observed after ex situ and in situ TEM mechanical testing. These results confirm the impact of SRO in Ti-Al alloys on the scale of angstroms. The direct confirmation of SRO in relationship to dislocation plasticity in metals can provide insight into how the mechanical behavior of concentrated solid solutions by the material's thermal history.

INTRODUCTION

The mechanical behavior of alloys is heavily influenced by the segregation of elements and atomic ordering within single-phase regions (*1*–*4*). Short-range ordering (SRO) describes the preferential local ordering of elements within a lattice, over spatial dimensions that are typically on the order of a few nearest neighbor spacings. In concentrated solid solutions, this phenomenon is known to strongly influence the dislocation dynamics and therefore the strength and ductility of an alloy (*5*–*8*). SRO is an equilibrium property of solid solutions and is an important phenomenon thought to exist in systems such as stainless steel (*9*) and medium/high-entropy alloys (M/HEAs) (*10*). In the titanium-aluminum binary system, the appearance of SRO has been hypothesized to trigger a "wavy to planar" slip transition, leading to localized planar deformation and, consequently, lower ductility and fracture toughness (*11*–*15*). Neeraj and Mills (*16*, *17*) reported that SRO causes anomalous hardening in aged Ti-6Al alloys and used transmission electron microscopy (TEM) to study its impact on the dislocation configurations. In samples that were aged to promote SRO formation, they found that leading dislocation pairs were observed at the tips of slip bands, which was hypothesized to result from the destruction and subsequent partial restoration of SRO (*5*, *12*). Residual strain in slip bands was later reported by weak-fringing analysis (*18*), which indicates the disturbance to the SRO structure caused by slip events. Van de Walle and Asta (*19*) used density functional theory–assisted Monte Carlo simulation to model SRO in α-phase Ti-Al alloys and calculate the diffuse antiphase boundary (DAPB) energies related to the disruption of local order by dislocation slip. To date, it is widely accepted that SRO is responsible to the anomalous strengthening and the lower ductility and fracture toughness in these materials, despite the lack of direct confirmation (*16*, *17*, *20*, *21*). Indirect evidence of SRO has been provided by Blackburn and Williams (*11*) via mechanical tests and Namboodhiri *et al.* (*22*) via resistivity measurements. More recently, studies confirmed the presence of SRO in Ti-6Al alloys by neutron diffraction experiments (*17*, *20*), in which weak and diffuse superlattice peaks were identified. These studies also revealed that the structure of the SRO domains is consistent with the α_2 phase (Ti_3Al, DO_{19} structure) (*23*), but they were not able to associate the SRO with deformation behavior through direct observation.

Despite the importance of SRO to the deformation behavior of structural alloys, the direct observation of SRO domains in those alloys has never been achieved. Conventional dark-field (DF) TEM imaging has been used in previous studies (*13*, *24*–*26*) to observe long-range ordering (LRO) in Ti-Al alloys, where α_2-phase precipitates formed with size above 10 nm. The direct imaging of SRO domains in this system has remained elusive due to their size and the diffuse nature of the local order. Therefore, it has not been possible to measure quantitative parameters such as the degree of local ordering and its characteristic spatial extent. In addition, without direct imaging, it is not possible to determine spatially resolved information such as the strain distribution and the interaction of dislocations with SRO domains. Here, we show that the SRO domain cluster structure can be directly imaged through experimental approaches and the associated quantitative parameters can be used to provide insight into deformation behaviors in Ti-6 weight % (wt %) Al alloy.

RESULTS AND DISCUSSION

For the experiments described below, Ti-6Al samples were homogenized at elevated temperature and then either directly water-quenched or aged at 420°C and then water-quenched to promote the formation of SRO (detailed aging, sample preparation, and experimental methods are provided in Materials and Methods). Both the as-quenched and SRO-aged samples were deformed for dislocation analysis. A clear trend of dislocation slip planarity in SRO-aged alloys is demonstrated in Fig. 1A, where near-screw oriented ⟨a⟩ type dislocations pile up along prismatic planes (the dislocation separation maximizes on an $[1\bar{2}10]$ orientation). In contrast, as-quenched samples show evenly distributed ⟨a⟩-type dislocations, as demonstrated in Fig. 1B. Unlike

[1]Department of Materials Science and Engineering, University of California, Berkeley, CA, USA. [2]National Center for Electron Microscopy, Molecular Foundry, Lawrence Berkeley National Laboratory, Berkeley, CA, USA. [3]Center of Modern Analysis, Nanjing University, Nanjing, Jiangsu, China. [4]Bruker Nano Surfaces, 9625 West 76th Street, Minneapolis, MN, USA. [5]Materials Sciences Division, Lawrence Berkeley National Laboratory, Berkeley, CA, USA.
*These authors contributed equally to this work.
†Corresponding author. Email: aminor@berkeley.edu

second-phase precipitation that can be commonly visualized with DF TEM, diffraction contrast from SRO is inherently diffuse due to the finite spatial extent and degree of the ordering. The diffuse nature and inhomogeneity of the SRO has proven to be a challenge for direct imaging with electrons in both imaging and diffraction modes. To address this issue, we used a Zeiss LIBRA 200MC microscope, equipped with an in-column Ω energy filter, Kohler illumination optics, and a high–dynamic range camera. Together, these instrument characteristics gave us the necessary signal-to-noise ratio to perform energy-filtered DF TEM imaging and visualize ultrafine SRO domains that give rise to diffuse electron diffraction (*27*–*29*). By using an energy filter, it is possible to enhance diffraction contrast (which is an elastic process) when the diffuse diffraction signal is similar to the diffuse background from inelastic scattering. In addition, the Kohler illumination characteristics (providing a more parallel primary beam in TEM mode versus conventional TEM imaging) resulted in a DF signal that was not possible to obtain in other state-of-the-art instruments also attempted with the same sample.

Using the Zeiss Libra TEM we performed energy-filtered DF imaging of the SRO domains (Fig. 2). Diffuse superlattice diffraction peaks can be visualized (Fig. 2C) and used to form an energy-filtered DF image as shown in Fig. 2A. This direct imaging enabled us to identify the predominant domains with enhanced order and characterize the distribution of their spatial sizes by using Gaussian template fitting (shown in higher magnification in Fig. 2B and with details of the analysis in Materials and Methods and the Supplementary Materials). In this analysis, we assume that the domains of enhanced order are spheres based on the DF images and the fact that there is no observable streaking in the diffraction pattern, leading to a reasonable measurement of the size of the bright domains. A histogram of the 7734 SRO domains identified by this analysis is plotted in Fig. 2D. The average size of the SRO domains identified in this way is $\bar{d}$ = 0.91 nm, with SD of σ = 0.27 nm. This size corresponds to ordering over a span of roughly two to three times the nearest-neighbor distance of the α-phase Ti (~2.95 Å), consistent with previous theoretical calculations that showed largest SRO parameters for first and second neighbor shells and decayed rapidly with further increases in distance (*19*). To further distinguish the SRO state from the early stage of LRO, energy-filtered diffraction patterns and DF images were also taken on the water-quenched sample and compared to the ones taken on the SRO-aged samples in fig. S6. The lack of clear superlattice peaks or DF contrast indicates that the ordering we observed is not from the quenching process but evolved during the annealing at 420°C. Geometrical phase analysis (GPA) on drift-corrected high-resolution scanning TEM (HRSTEM) (*30*) images showed a subnanometer-sized strain fluctuation in SRO-aged samples, revealing the lattice distortion caused by the lattice mismatch of the bright domains (a strain map is plotted in fig. S3).

The average size and volume fraction of secondary phases are known to play a potent role in the mechanical properties of precipitation-strengthened alloys as they can strongly hinder dislocation motion (*31*). However, in the case of SRO, the effect on the mechanical properties has only been discussed qualitatively. With both the energy-filtered DF image and experimental measurement of the sample thickness, we have calculated the volume fraction of bright domains identified through the DF analysis and the fraction of Al atoms that are in the ordered status in these domains. The volume fraction of SRO domains is 1.25%. If we assume that all of the bright domains are in the fully ordered DO_{19} structure, then there are only 3.11% of all Al atoms at the ordered positions in these domains. This unique parameter emphasizes the thermal condition that the SRO status is established, where only short-range diffusion is realized by a relatively small fraction of the total Al atoms in the alloy.

To assess the impact of SRO on the mechanical properties of the alloy, bulk compression tests were conducted on the as-quenched and SRO-aged samples. The stress-strain curves are presented in Fig. 3A. In the case of the bulk mechanical test, SRO has almost no impact on the alloy's Young's modulus, indicating very little effect on elastic properties. The yielding behavior, however, is significantly altered.

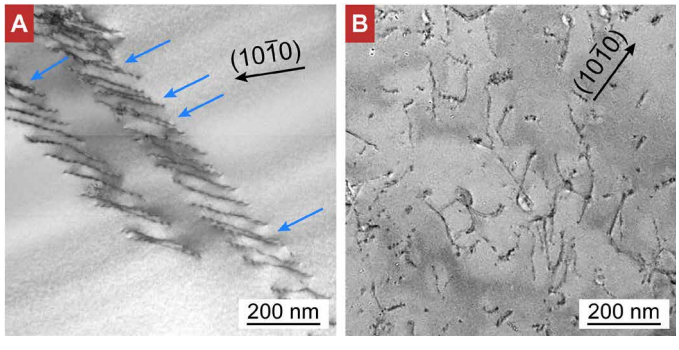

Fig. 1. TEM bright-field imaging of deformed Ti-6Al with different thermal history. (**A**) Sample aged to promote SRO; the blue arrows mark the in-band dislocation pairs. (**B**) Sample quenched after homogenization.

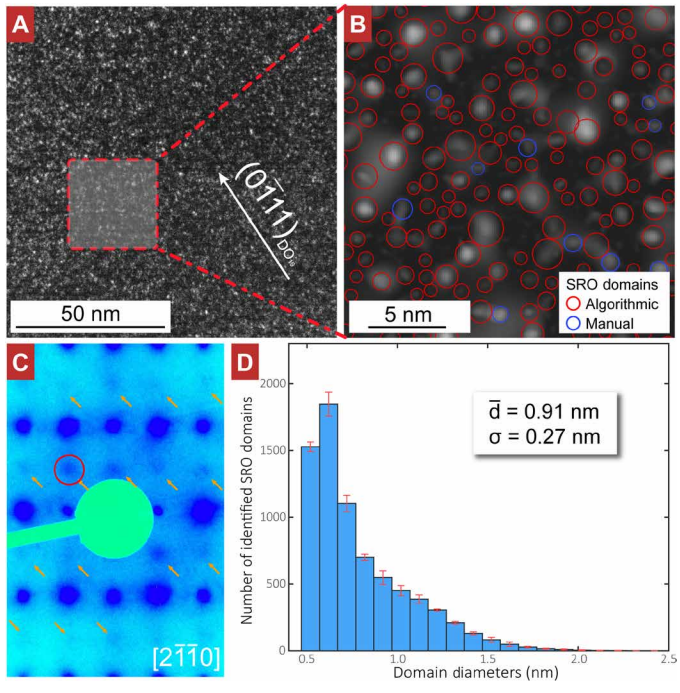

Fig. 2. Energy-filtered DF imaging of SRO domains. (**A**) The energy-filtered DF image from superlattice diffraction shows distinguishable SRO domains. (**B**) Enlarged DF image with identified SRO domains marked by the red circles; the circles are scaled larger than the measured radius. (**C**) Energy-filtered $[2\bar{1}\bar{1}0]$ diffraction pattern. The orange arrows indicate the positions of the diffuse DO_{19} superlattice diffraction peaks. The red circle marks the objective aperture position used in (A). (**D**) Size distribution of the identified SRO domains from three DF images (enlarged images are shown in fig. S7); the error bars were assigned according to the SD among three similar images.

As demonstrated in Fig. 3B, the stress-strain curve of the SRO-aged sample is strongly jagged with a well-defined yield point. Comparatively, the as-quenched sample exhibited a smooth yield. Presumably, the upper yield point in the SRO-aged sample is a result of the onset of planar slip events, where only the leading dislocations experience the high energy barrier associated with the creation of DAPB. Through an analogous mechanism to the creation of antiphase boundaries in a LRO alloy, a mechanism first proposed by Fisher (*5*) would result in a relatively high interface energy that strongly hinders initial dislocation motion. Van de Walle and Asta calculated that the DAPB energy of SRO Ti-Al alloy is ~25 mJ/m^2 for a system containing 10 atomic % Al, which is significantly lower than the APB energy of the ordered Ti_3Al alloy (*19*). With the calculated domain size for regions of enhanced order and the volume fraction, we can provide an estimation of the hardening caused by SRO based on a classical model of ordered precipitation hardening mechanism (*32*, *33*), where the bright domains are treated as ordered obstacles to a first approximation

$$\Delta\sigma_y = M \cdot 0.81 \frac{\gamma_{DAPB}}{2b}\left(\frac{3\pi}{8}\varphi_{SRO}\right)^{\frac{1}{2}} \quad (1)$$

where $M \sim 3$ is the Taylor factor for polycrystalline materials, 0.81 is a geometrical factor, γ_{DAPB} is the diffuse anti-phase boundary energy, φ_{SRO} is the volume fraction of bright domains, b is the norm of a Burgers vector, and r is the measured radius of the domains. The calculated $\Delta\sigma_y$ is ~12 MPa. As demonstrated in Fig. 3B, the measured yield stress, taken at the 0.2% strain offset, indicates that the SRO alloy is ~22 MPa stronger than its homogeneous counterpart, which matches reasonably well with our calculation, especially without the consideration of other strengthening mechanisms such as solute and cluster hardening.

In addition to a yield-point increase, the formation of SRO leads to localized deformation through a strong pinning effect from the domains. This effect can be demonstrated by probing the localized deformation during the initial stages of a nanoindentation test. We performed nanoindentation tests in the dynamic mechanical analysis (DMA) mode on both SRO-aged and as-quenched samples with strong prismatic texture. The indentation stress-strain curves are plotted in Fig. 3 (C and D). The sample surfaces were electrochemically polished and can be considered dislocation free before testing. Despite the occasional appearances of small pop-ins, a relatively continuous elastic-plastic deformation response was observed for the as-quenched

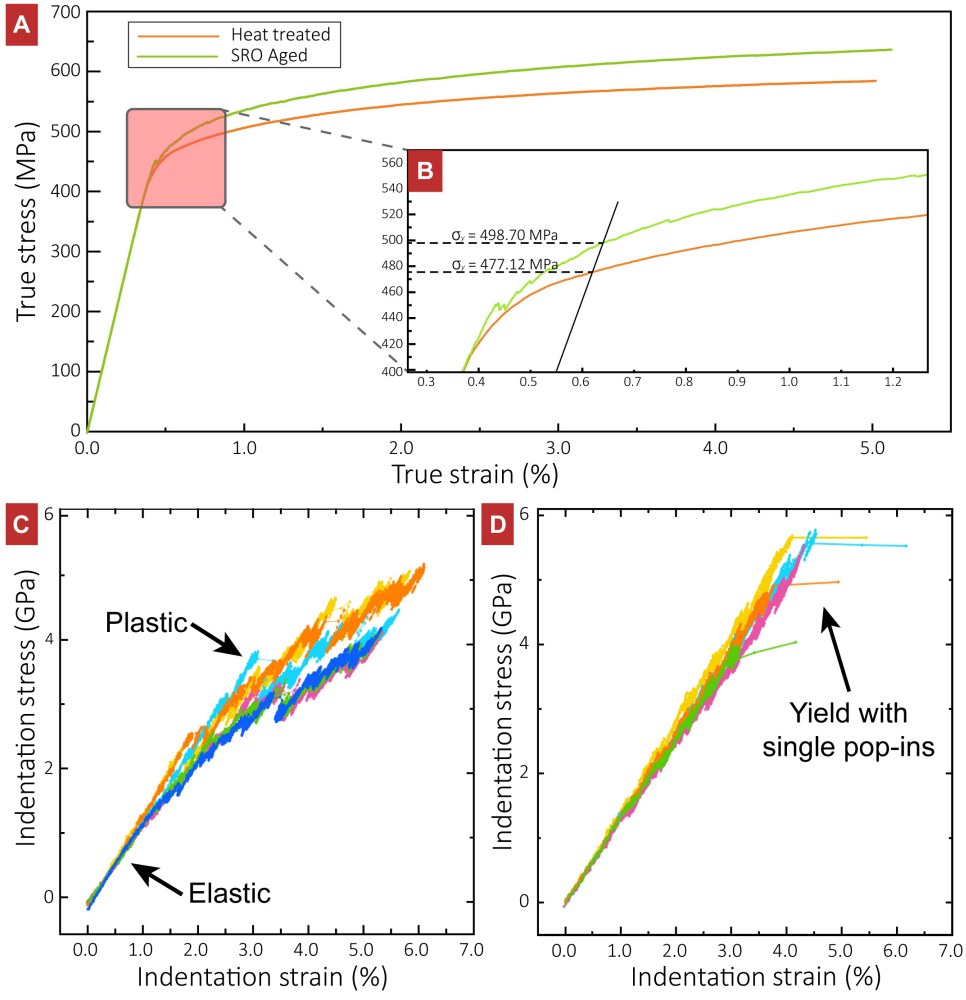

Fig. 3. Comparison of the mechanical response of Ti-6Al in the quenched and SRO-aged conditions. (**A**) True stress-strain curves of the quenched and SRO-aged samples. (**B**) Enlarged true stress-strain curves near yielding of both materials; the 0.2% offset yield strength is marked on the plot. (**C** and **D**) Indentation stress-strain curves of as-quenched sample and SRO-aged sample, respectively. Different indentations are marked with different colors.

alloy, whereas in the SRO-aged sample, dramatic pop-ins occur at high stress state, indicating dislocation avalanches. The dramatic change in the yielding behavior of localized deformation is consistent with the hypothesis that the presence of SRO leads to higher initial yielding, but once an SRO-free slip band is established, dramatic strain softening occurs (here seen via a nanoindentation pop-in). Because of the delayed feedback control of the instrument and the dependency of the nanoindentation stress-strain curves on the area function, the data after the large pop-ins in Fig. 3D have been truncated to avoid any confusion about the origin of the excursions.

After initial yielding, the destruction of SRO leads to relatively two-dimensional (2D) plasticity through the promotion of relatively soft regions (so-called planar slip behavior). Because of the direct-imaging of enhanced SRO domains made possible with energy-filtered electron diffraction, the destruction of SRO in planar slip bands can be directly verified. Figure 4A shows a slip band with residual strain contrast and the associated DF image using the same superlattice imaging condition shown in Fig. 2. As marked in Fig. 4B, individual SRO domains are visible in the entire frame. However, there are fewer SRO domains in the slip band. The contrast is likely due to the fact that SRO-enhanced domains on the slip band were cut through and destroyed by dislocation motion. Further verification of the decrease in SRO-enhanced domains within a single slip band was provided by energy-filtered quantitative electron diffraction (QED) imaging (see fig. S1).

To directly correlate the destruction of SRO with deformation, in situ nanopillar compression tests were conducted on an FEI TitanX TEM with a Bruker PI-95 picoindenter. The orientation of the pillars was aligned to favor prismatic slip (schematic is provided in movie S1). The energy-filtered diffraction patterns were acquired in the Zeiss LIBRA 200MC microscope before and after the deformation tests. One example of the tests is shown in Fig. 5. During the compression, a relatively homogeneous deformation at the tip region was produced by the indenter. Planar dislocation pileups developed during the test as shown in movie S2. The energy-filtered diffraction patterns taken from the tip of the pillars show the change of microstructure caused by the plasticity. Initially, the SRO diffuse superlattice diffraction peaks are visible, whereas after the deformation, the corresponding peaks disappeared. The effect was quantified in the diffraction intensity line plots in Fig. 5. In principle, the localized prismatic planar slip would only interrupt SRO in a limited zone. Nevertheless, in the case of in situ nanopillar compression, the severe and relatively homogeneous deformation was enough to diminish the superlattice diffraction peaks to below the noise level.

A well-accepted concept of the planar slip is that the successive dislocations glide along a single atomic plane due to the glide plane softening effect caused by the leading dislocations interrupting the SRO and subsequently lowering the energy barrier for following dislocations. Nevertheless, a dislocation slip trace analysis shows that adjacent dislocations in a planar slip band were actually gliding on separated $(1\bar{1}00)$ planes. The results are shown in fig. S2. Furthermore, dislocation pairs were not only observed at the leading dislocations but also among following dislocations mid-band (as marked in Fig. 1A). A similar phenomenon was also observed in previous studies (*16*, *17*, *21*, *25*) but not discussed in detail. The leading pairs of dislocations are caused by the creation and partial restoring of the DAPB by the leading dislocations, making them closer to each other to lower the DAPB energy. Such pairing was directly related to the existence of SRO (*16*, *17*, *19*, *25*). Considering the size of the bright

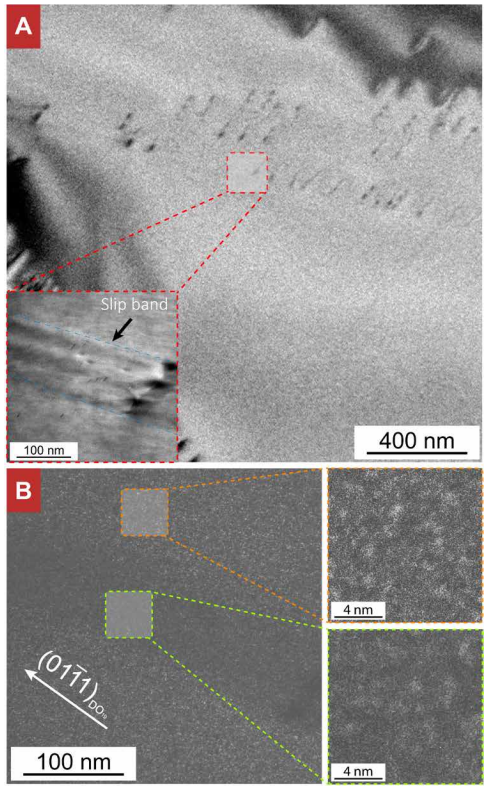

Fig. 4. Energy-filtered DF images of planar dislocation slip bands. (**A**) Bright-field image showing the relation of a slip band and the imaging area. The slip band is marked and shows weak-fringing contrast in the zoomed-in image. (**B**) Energy-filtered DF image at the same position of (A) showing the lack of contrast in the slip band.

domains, only one or two pairs would entirely destroy the ordering in a certain slip band, and it is unlikely that the SRO in the case of substitutional solutes such as Al in Ti would be restored through diffusion during room temperature deformation. Therefore, the pairing we observed in the middle of the slip band is consistent with the idea that the dislocations might have cross slipped to adjacent planes and repeated the pairing process on the new plane, assuming that the dislocations in the slip band are from the same source. If so, the result would be that the planar slip is delocalized to a thin 3D zone instead of a 2D slip plane, which is consistent with the relatively wide band of depleted bright domains seen in Fig. 4B.

Considering the process further, we note that the observed dominant deformation mechanism in these experiments is ⟨a⟩-type dislocation slip. In Ti-6Al, the screw components of the observed ⟨a⟩-type dislocations can glide on basal, prismatic, and pyramidal planes (*15*, *34*–*36*). Our experimental observations would thus suggest that the barrier for reconfiguration of the ⟨a⟩-type dislocation cores is relatively small such that dislocations could move on these other slip planes to cross-slip to adjacent prismatic planes. We propose that the delocalized planar slip is a combined result of the repulsive interactions among dislocations, cross-slip of ⟨a⟩-type dislocations, the higher mobility on prismatic planes, and the glide plane softening caused by the local strain field. Further studies are needed to understand the exact contributions of these mechanisms to the width of a shear plane.

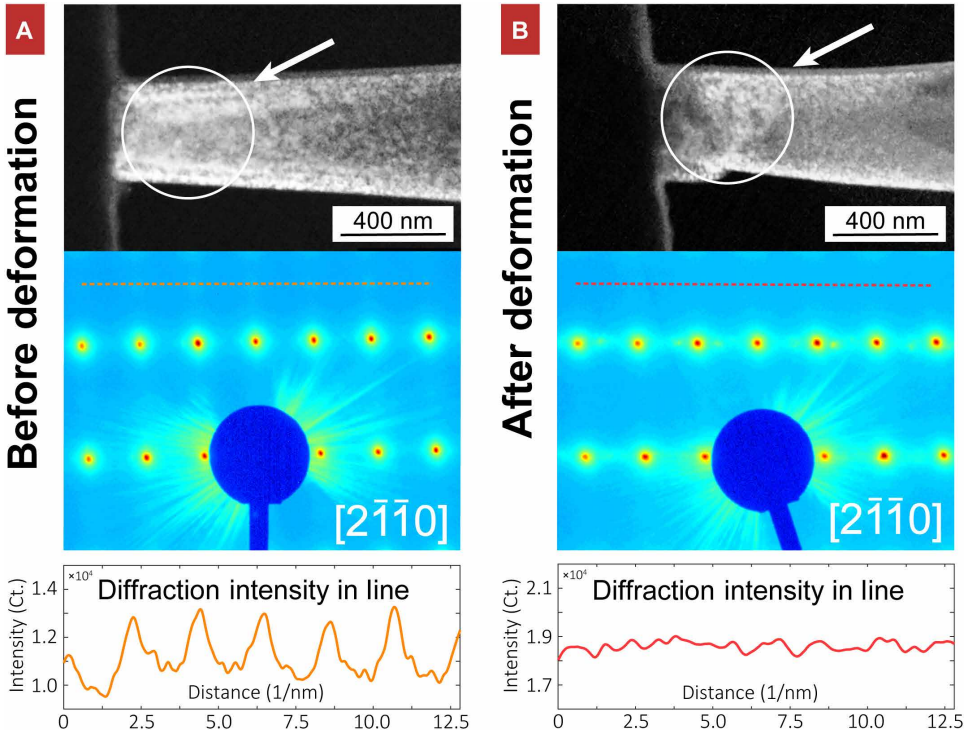

Fig. 5. Diffraction analysis of TEM in situ compression test on a nanopillar made from an SRO-aged sample. (**A**) DF image, diffraction pattern, and superlattice diffraction intensity line plot from before the in situ compression test. The position of the line plot is marked on the diffraction pattern. (**B**) DF image, diffraction pattern, and superlattice diffraction intensity line plot from after the in situ compression test. The position of the line plot is marked on the diffraction pattern. After the deformation, the diffuse superlattice peaks decreased beneath the noise level, presumably caused by the destruction of SRO at the tip region due to the dislocation activities.

CONCLUSIONS

In the current study, the SRO in Ti-6Al system was directly imaged via energy-filtered DF imaging, revealing the domain cluster microstructure of SRO. This structure is formed by short-range diffusion that results in localized atomic reconfiguration. The size distribution and the total volume fraction of the enhanced SRO domains were measured and related to the alloy's mechanical properties. Microstructurally, the interaction of dislocations and domains of enhanced order was probed through both in situ and postmortem TEM observations, showing that the domains were destroyed by dislocation plasticity. In addition, the remaining domains in a slip band rendered a weaker contrast in the DF image, suggesting the existence of a strain field left by the slip events. A unique aspect of the observed "planar slip" is that the slip band is delocalized to adjacent prismatic planes, leaving a thin 3D zone rather than a single glide plane free of SRO domains. This broadening of the slip band is evidence of cross slip of ⟨a⟩-type dislocations, which should be promoted by the relatively low value of the DAPB energy. The unique structure of dislocation cores in Ti (*34*), which creates a tendency for the cores to spread on pyramidal planes, also increases the chance of cross slip, although further investigation is needed to validate the trend in Ti-6Al alloy. Considering the repulsive interactions among the dislocation pileups, delocalization of the planar slip could be achieved through small stress-driven pyramidal slip. SRO increases the critical resolved shear stress of a dislocation on its slip planes and hence increases the nominal yield stress, which is confirmed by our bulk uniaxial compression test. A simple model based on the DAPB strengthening was proposed to estimate the stress increment, and it matches reasonably well with the experimental results. It is worth mentioning that the current study focuses on the deformation of ⟨a⟩-type dislocation slip. The consequences of SRO for ⟨c + a⟩-type slip or twinning, which are required to accommodate *c*-axis deformation, have not been investigated in this work. Such further investigations would be of interest to achieve a more complete picture of SRO on the intrinsic plastic anisotropy in hcp-Ti alloys.

In summary, through direct visualization of the SRO structure in and around shear bands in Ti-6Al, we have verified the concept that DAPBs play an essential role in alloy plasticity. The methods developed in the current study could potentially be applied to other SRO-forming systems such as M/HEAs, for instance, where SRO could be an important factor underlying their excellent combination of strength, ductility, and fracture toughness (*37*–*40*).

MATERIALS AND METHODS

Sample preparation

The material used in this research was provided by TIMET, UK. The raw material was argon arc double melted and then forged to square at 1125°C before water quenching. The square was then rolled at 910°C. The composition of the ingot material is Ti with 6 wt % Al and 0.05 wt % O. The oxygen content is due to the processing. The buttons were heat-treated at 965°C for 2 hours (~45°C below the β-transus) to give a strain-free equiaxed microstructure. A portion of the material was further aged at 420°C for 1 week to promote the SRO. The grain sizes of both heat-treated and aged samples were measured by electron backscatter diffraction (EBSD) to be ~50 μm. Samples for dislocation analysis went through a room temperature bulk compression test that was carried out on an MTS Criterion

(Model 43) system to introduce dislocation plasticity. The final strain was 6%, with a strain rate of 1×10^{-3}. The material was then sliced and thinned by mechanical polishing. Samples for TEM and in situ TEM experiments were polished with the Fischione Twin Jet Electropolisher (Model 110) to electron transparency using a solution of 6% perchloric acid and 94% methanol at −40°C at approximately 30 V. The nanopillars for the TEM in situ compression experiments were further prepared on an FEI Strata 235 dual-beam focused ion beam (FIB) system via FIB cutting. The samples for DMA nanoindentation were prepared by mono-side electrochemical polishing with aforementioned solution and parameters.

Dislocation analysis

TEM dislocation analysis was conducted on both aged and as-quenched samples with compressive deformation. The TEM observation was conducted on the FEI TitanX and the JEOL 3010 operating at 300 kV at the National Center for Electron Microscopy (NCEM), Lawrence Berkeley National Laboratory. "g dot b" and trace analysis were carried out to identify the type and slip direction of the dislocations. HRSTEM was conducted on the TEAM I microscope (300 kV) at NCEM to identify the glide-plane relations of adjacent dislocations.

Energy-filtered DF TEM imaging and SRO domain recognition

TEM samples of aged Ti-6Al alloys were used for the observation. A Zeiss LIBRA 200MC microscope, equipped with an in-column Ω energy filter, was used to take both diffraction patterns and DF images. A 5-eV energy slit was deployed to select the zero-loss peak and eliminate the contrast from inelastic scattering. A Gatan US1000 charge-coupled device camera with exposure times of 15 s was used to acquire the diffraction patterns. The SRO domains were assumed to be spherical, which is consistent with the circular nature of the diffuse superlattice peaks showing lack of preferred orientation. Domains of enhanced order were identified and measured through Gaussian template fitting. The detailed algorithm and the optimization of identification parameters are summarized in the Supplementary Materials. A manual inspection was conducted afterward to identify the missed domains. To further validate the measurement, the particle analysis tool provided by ImageJ package (based on threshold segmentation algorithm) was used, yielding an average domain size of ~0.86 nm, which matches well with our template fitting method.

The sample thickness was carefully measured by performing a FIB cross section of the interested TEM sample. The thickness profile is summarized in fig. S4, where the sample thickness of the interested area was measured to be ~25 nm. With it, the measured domain number was further calibrated by considering the shadowing effect through the sample thickness. A 124 × 124 × 28 mesh was created according to the DF image frame size and the identified mean domain size (~0.91 nm). A Monte Carlo algorithm was implemented to fill the mesh and match the visible count of domains. The total domain numbers were averaged through 100 iterations, and the SD was calculated to ensure an accurate result.

Spherical nanoindentation and indentation stress-strain curves

The nanoindentation tests were conducted on a Bruker Ti 950 TriboIndenter instrument with a 10-μm spherical tip in DMA mode. After mechanical polish, both aged and as-quenched Ti-6Al bulk samples were electrochemically polished with a solution of 6% perchloric acid and 94% methanol at −40°C, with a voltage of approximately 30 V. The finished surface showed, as confirmed by EBSD scans, a strong prismatic texture. The detailed procedures to convert raw indentation data into ISS curves have been well documented in previous reports (*41*–*43*). All indentation sites were carefully chosen to avoid grains with near-basal orientation and regions near grain boundaries.

In situ TEM nanopillar compression

The nanopillars were made with a FIB system as previously elaborated. The in situ compression tests were performed on an FEI TitanX TEM with a Bruker PI-95 picoindenter. The samples, oriented 45° from the *c* axis to maximize the shear stress on prismatic glide planes, were made approximately 200 nm in diameter and 600 nm in length. The energy-filtered diffraction patterns were taken with a Zeiss LIBRA 200MC microscope before and after the deformation tests.

Diffraction contrast imaging via virtual-aperture reconstruction

To image the effect of dislocation motion on the bright domains, a tilt series of zero-loss filtered DF images were recorded, using the QED plug-in for Digital Micrograph that allows automatic control of the electron beam, in a Zeiss Libra 200MC microscope at 200 kV. As demonstrated by Gammer *et al.* (*44*), the beam tilt series, in reciprocal space, was set in a circular region defined by a maximum tilt angle. The diffraction resolution was determined by the tilt spacing of the tilting grid. The resulting data, composed of a set of DF images associated to a specific beam tilt angle, were then aberration-corrected by the QED plug-in. The images were aligned by cross-correlation to compensate for sample drift during the data acquisition. A virtual diffraction pattern was generated by assigning the mean intensity of individual DF image to the associated tilt position. Virtual objective apertures could be placed anywhere in the virtual diffraction pattern, and the DF image would be reconstructed by summing the images from the specified tilt defined by the apertures. In this research, multiple virtual objective apertures were used to pick up signals from SRO diffuse peaks.

HRSTEM imaging and GPA

HRSTEM imaging of SRO-aged samples, both with (for slip trace analysis) and without (for GPA analysis) deformation, was also conducted at NCEM on the double-corrected TEAM I microscope operated at 300 kV. Drift correction was conducted with the methods developed by Ophus *et al.* (*30*) to eliminate the artifacts from beam scan jittering. FRWRtools were used for the following GPA analysis. Averaged fast Fourier transforms were used as strain templates. The real-space resolution was set to 1.5 nm to get a relatively accurate measurement in reciprocal space.

SUPPLEMENTARY MATERIALS

Supplementary material for this article is available at http://advances.sciencemag.org/cgi/content/full/5/12/eaax2799/DC1

Supplementary Text

Fig. S1. Diffraction contrast showing the destruction of SRO clusters in a slip band using QED.

Fig. S2. Dislocation slip trace analysis conducted with HRSTEM imaging.

Fig. S3. GPA of an SRO-aged sample and a high-purity Ti sample.

Fig. S4. Cross-section thickness measurement of the TEM sample imaged in Fig. 2.

Fig. S5. Parameter optimization of the SRO domain identification algorithm.

Fig. S6. Diffraction patterns and DF images of samples with different thermal histories.
Fig. S7. Energy-filtered DF images showing SRO-enhanced domains.
Movie S1. Schematic of the in situ pillar compression test.
Movie S2. One example of the in situ pillar compression.

REFERENCES AND NOTES

1. P. A. Flinn, Solute hardening of close-packed solid solutions. *Acta Metall.* **6**, 631–635 (1958).
2. J. C. Kim, N. H. Heo, J. G. Na, J. S. Woo, G. M. Kim, Effects of silicon addition on grain boundary segregation behaviors and mechanical properties in α-iron. *Scr. Mater.* **38**, 1071–1076 (1998).
3. M. Bugnet, A. Kula, M. Niewczas, G. A. Botton, Segregation and clustering of solutes at grain boundaries in Mg-rare earth solid solutions. *Acta Mater.* **79**, 66–73 (2014).
4. L. Zou, C. Yang, Y. Lei, D. Zakharov, J. M. K. Wiezorek, D. Su, Q. Yin, J. Li, Z. Liu, E. A. Stach, J. C. Yang, L. Qi, G. Wang, G. Zhou, Dislocation nucleation facilitated by atomic segregation. *Nat. Mater.* **17**, 56–62 (2018).
5. J. C. Fisher, On the strength of solid solution alloys. *Acta Metall.* **2**, 9–10 (1954).
6. J. B. Cohen, M. E. Fine, Some aspects of short-range order. *J. Phys. Radium* **23**, 749–762 (1962).
7. J. B. Cohen, M. E. Fine, A new method for the detection of short-range order. *Acta Metall.* **11**, 1106–1109 (1963).
8. V. Gerold, H. P. Karnthaler, On the origin of planar slip in f.c.c. alloys. *Acta Metall.* **37**, 2177–2183 (1989).
9. T. C. Pekin, C. Gammer, J. Ciston, C. Ophus, A. M. Minor, In situ nanobeam electron diffraction strain mapping of planar slip in stainless steel. *Scr. Mater.* **146**, 87–90 (2018).
10. Y. Ma, Q. Wang, C. Li, L. J. Santodonato, M. Feygenson, C. Dong, P. K. Liaw, Chemical short-range orders and the induced structural transition in high-entropy alloys. *Scr. Mater.* **144**, 64–68 (2018).
11. M. J. Blackburn, J. C. C. Williams, Strength, deformation modes and fracture in Ti-Al alloys. *Trans. ASM* **62**, 398–408 (1969).
12. H. Conrad, On the strengthening of titanium by aluminum. *Scr. Metall.* **7**, 509–512 (1973).
13. D. J. Truax, C. J. McMahon, Plastic behavior of titanium-aluminum alloys. *Mater. Sci. Eng.* **13**, 125–139 (1974).
14. J. C. Williams, G. Luetjering, in *Effect of Slip Length and Slip Character on the Properties of Titanium Alloys*, O. Kimura, H. Izumi, Eds. (TMS-AIME, 1981), vol. 1, pp. 671–681.
15. G. Lütjering, J. C. Williams, *Titanium* (Springer, 2003).
16. T. Neeraj, D.-H. Holc, G. S. Daehn, M. J. Mills, Phenomenological and microstructural analysis of room temperature creep in titanium alloys. *Acta Mater.* **48**, 1225–1238 (2000).
17. T. Neeraj, M. J. Mills, Short-range order (SRO) and its effect on the primary creep behavior of a Ti-6wt.%Al alloy. *Mater. Sci. Eng. A* **319–321**, 415–419 (2001).
18. T. Neeraj, M. J. Mills, Observation and analysis of weak-fringing faults in ti-6 wt% al. *Philos. Mag. A* **82**, 779–802 (2002).
19. A. Van De Walle, M. Asta, First-principles investigation of perfect and diffuse antiphase boundaries in HCP-based Ti-Al alloys. *Metall. Mater. Trans. A* **33**, 735–741 (2002).
20. A. Fitzner, D. G. L. Prakash, J. Q. Fonseca, M. Thomas, S.-Y. Zhang, J. Kelleher, P. Manuel, M. Preuss, The effect of aluminium on twinning in binary alpha-titanium. *Acta Mater.* **103**, 341–351 (2016).
21. P. Castany, F. Pettinari-Sturmel, J. Douin, A. Coujou, TEM quantitative characterization of short-range order and its effects on the deformation micromechanims in a Ti-6Al-4V alloy. *Mater. Sci. Eng. A* **680**, 85–91 (2017).
22. T. K. G. Namboodhiri, C. J. McMahon, H. Herman, Decomposition of the α-phase in titanium-rich Ti-Al alloys. *Metall. Trans. A.* **4**, 1323–1331 (1973).
23. Y. Minonishi, Plastic deformation of single crystals of Ti 3 Al with D0 19 structure. *Philos. Mag. A.* **63**, 1085–1093 (1991).
24. J. C. Williams, R. G. Baggerly, N. E. Paton, Deformation behavior of HCP Ti-Al alloy single crystals. *Metall. Mater. Trans. A.* **33**, 837–850 (2002).
25. A. Radecka, J. Coakley, I. P. Jones, D. Rugg, T. C. Lindley, D. Dye, Ordering and the micromechanics of Ti-7Al. *Mater. Sci. Eng. A* **650**, 28–37 (2016).
26. A. Radecka, J. Coakley, V. A. Vorontsov, T. L. Martin, P. A. J. Bagot, M. P. Moody, D. Rugg, D. Dye, Precipitation of the ordered α2phase in a near-α titanium alloy. *Scr. Mater.* **117**, 81–85 (2016).
27. D. Shindo, A. Gomyo, J.-M. Zuo, J. C. H. Spence, Short-range ordered structure of Ga0. 47In0. 53 as studied by energy-filtered electron diffraction and HREM. *J. Electron Microsc.* **45**, 99–104 (1996).
28. Y. Ikematsu, D. Shindo, T. Oikawa, Quantitative analysis of short-range order diffuse scattering in Cu-27.5 at%Pd alloy with energy-filtered electron diffraction. *Mater. Trans. JIM* **41**, 238–241 (2000).
29. T. Yano, Y. Murakami, D. Shindo, S. Kuramoto, Study of the nanostructure of Gum Metal using energy-filtered transmission electron microscopy. *Acta Mater.* **57**, 628–633 (2009).
30. C. Ophus, J. Ciston, C. T. Nelson, Correcting nonlinear drift distortion of scanning probe and scanning transmission electron microscopies from image pairs with orthogonal scan directions. *Ultramicroscopy* **162**, 1–9 (2016).
31. K. M. Ralls, T. H. Courtney, J. Wulff, *Introduction to Materials Science and Engineering* (Wiley, 1976).
32. A. J. Ardell, Precipitation hardening. *Metall. Trans. A.* **16**, 2131–2165 (1985).
33. T. Gladman, Precipitation hardening in metals. *Mater. Sci. Technol.* **15**, 30–36 (1999).
34. E. Clouet, D. Caillard, N. Chaari, F. Onimus, D. Rodney, Dislocation locking versus easy glide in titanium and zirconium. *Nat. Mater.* **14**, 931–936 (2015).
35. V. Hasija, S. Ghosh, M. J. Mills, D. S. Joseph, Deformation and creep modeling in polycrystalline Ti-6Al alloys. *Acta Mater.* **51**, 4533–4549 (2003).
36. R. I. Jaffee, The physical metallurgy of titanium alloys. *Prog. Met. Phys.* **7**, 65–163 (1958).
37. J. Ding, Q. Yu, M. Asta, R. O. Ritchie, Tunable stacking fault energies by tailoring local chemical order in CrCoNi medium-entropy alloys. *Proc. Natl. Acad. Sci. U.S.A.* **115**, 201808660 (2018).
38. J.-W. Yeh, S.-K. Chen, S.-J. Lin, J.-Y. Gan, T.-S. Chin, T.-T. Shun, C.-H. Tsau, S.-Y. Chang, Nanostructured high-entropy alloys with multiple principal elements: Novel alloy design concepts and outcomes. *Adv. Eng. Mater.* **6**, 299–303 (2004).
39. B. Cantor, I. T. H. Chang, P. Knight, A. J. B. Vincent, Microstructural development in equiatomic multicomponent alloys. *Mater. Sci. Eng. A* **375–377**, 213–218 (2004).
40. Y. Zhang, T. T. Zuo, Z. Tang, M. C. Gao, K. A. Dahmen, P. K. Liaw, Z. P. Lu, Microstructures and properties of high-entropy alloys. *Prog. Mater. Sci.* **61**, 1–93 (2014).
41. S. Pathak, S. R. Kalidindi, Spherical nanoindentation stress–strain curves. *Mater. Sci. Eng. R* **91**, 1–36 (2015).
42. S. J. Vachhani, S. R. Kalidindi, Grain-scale measurement of slip resistances in aluminum polycrystals using spherical nanoindentation. *Acta Mater.* **90**, 27–36 (2015).
43. S. J. Vachhani, R. D. Doherty, S. R. Kalidindi, Studies of grain boundary regions in deformed polycrystalline aluminum using spherical nanoindentation. *Int. J. Plast.* **81**, 87–101 (2016).
44. C. Gammer, V. Burak Ozdol, C. H. Liebscher, A. M. Minor, Diffraction contrast imaging using virtual apertures. *Ultramicroscopy* **155**, 1–10 (2015).

Acknowledgments

Funding: We gratefully acknowledge funding from the U.S. Office of Naval Research under grant no. N00014-16-1-2304. Work at the Molecular Foundry was supported by the Office of Science, Office of Basic Energy Sciences, of the U.S. Department of Energy under contract no. DE-AC02-05CH11231. We thank J. Wu for help on sample heat treatment. **Author contributions:** R.Z., A.M.M., S.Z., J.W.M., D.C.C., and M.A. prepared the manuscript, which was reviewed and edited by all authors; C.O. and R.Z. developed and optimized the domain recognition algorithm; Y.D. and R.Z. conducted the in situ TEM compression experiments; S.J.V. and R.Z. conducted the nanoindentation tests; B.O. and R.Z. conducted the QED experiments; R.T. developed the heat treatment method; K.C.B. and R.Z. conducted the energy-filtered TEM imaging; S.Z. and R.Z. conducted the bulk compression tests; S.Z. conducted the quantitative analysis of mechanical properties. Project administration, supervision, and funding acquisition were performed by M.A., D.C.C., J.W.M., and A.M.M. **Competing interests:** The authors declare that they have no competing interests. **Data and materials availability:** All data needed to evaluate the conclusions in the paper are present in the paper and/or the Supplementary Materials. Additional data related to this paper may be requested from the authors.

Submitted 9 March 2019
Accepted 29 October 2019
Published 13 December 2019
10.1126/sciadv.aax2799

Citation: R. Zhang, S. Zhao, C. Ophus, Y. Deng, S. J. Vachhani, B. Ozdol, R. Traylor, K. C. Bustillo, J. W. Morris Jr., D. C. Chrzan, M. Asta, A. M. Minor, Direct imaging of short-range order and its impact on deformation in Ti-6Al. *Sci. Adv.* **5**, eaax2799 (2019).